J Mater Sci (2014) 49:2403–2414
DOI 10.1007/s10853-013-7852-1

Influence of microstructural heterogeneity on the scaling between flow stress and relative density in microcellular Al–4.5 %Cu

Yves Conde · Roberto Doglione · Andreas Mortensen

Received: 6 September 2013 / Accepted: 29 October 2013 / Published online: 3 January 2014

Abstract We explore the influence of the metal microstructure on the compressive flow stress of replicated microcellular 400-μm pore size Al–4.5 wt%Cu solidified at two different solidification cooling rates, in the as-cast and T6 conditions. It is found that the yield strength roughly doubles with age-hardening, but does not depend on the solidification cooling rate. Internal damage accumulation, measured by monitoring the rate of stiffness loss with strain, is similar across the four microstructures explored and equals that measured in similar microcellular pure aluminium. In situ flow curves of the metal within the open-pore microcellular material are back-calculated using the Variational Estimate of Ponte-Castañeda and Suquet. Consistent results are obtained with heat-treated microcellular Al–4.5 wt%Cu and are also obtained with separate data for pure Al; however, for the as-cast microcellular Al–4.5 wt%Cu, the back-calculated in situ metal flow stress decreases, for both solidification rates, with decreasing relative density of the foam. We attribute this effect to an interplay between the microstructural and mesostructural features of the microcellular material: variations in the latter with the former held constant can alter the scaling between flow stress and relative density within microcellular alloys.

Y. Conde (✉) · R. Doglione · A. Mortensen
Laboratoire de Métallurgie Mécanique, Institut des Matériaux,
Ecole Polytechnique Fédérale de Lausanne, Station 12,
1015 Lausanne, Switzerland
e-mail: yves.conde@constellium.com

A. Mortensen
e-mail: andreas.mortensen@epfl.ch

Present Address:
Y. Conde
Constellium, EPFL - Quartier de l'Innovation, Bâtiment E,
1015 Lausanne, Switzerland

R. Doglione
INSTM, Via G, Giusti 9, 50121 Florence, Italy

Introduction

Replicated microcellular aluminium is made by producing a porous preform of bonded NaCl powder for subsequent infiltration with aluminium or one of its alloys [1, 2]. After metal solidification, the NaCl preform is removed by dissolution in water to create a fine interconnected network of metal. The packed NaCl particle bed gives pores of the material their shape or in other words defines the microcellular material's mesostructure. Its microstructure is, on the other hand, defined by the alloy composition and by internal features of its constituent metal or alloy.

Both the mesostructure and the microstructure are known to influence the properties of microcellular metals or alloys; general reviews of structure/property relations in those materials can be found in Refs. [2–4]. At high porosity, the influence of the mesostructure is dominant: variations in the architecture of microcellular metal can change their general load-bearing capacity in both the elastic or plastic deformation by several orders of magnitude (for illustration of this sees Figs. 17 and 18 of Ref. [5] and Figs. 5 to 7 of Ref. [6]). The microstructure, on the other hand, exerts its influence by changing intrinsic properties of the solid metal or alloy making the microcellular material at hand. Microstructure variations will thus generally not change dramatically the elastic modulus of microcellular metals (since the stiffness of most engineering alloys is relatively insensitive to microstructure or composition), but will influence the strength of microcellular metals significantly, a priori in equal proportion to what is observed in dense metals and alloys. This is,

for example, visible in the fact that significant increases in flow stress can be produced in microcellular metals by heat-treatment if their constituent metal alloy is an age-hardening alloy [7–18]. Harnessing the microstructure of microcellular metals is thus an interesting way of optimizing their strength.

A question this raises is whether processing-microstructure-strength relations remain the same, in microcellular metals or alloys, as in the same metal or alloy when it is dense. Often, this is not so: Thornton and Magee showed in their pioneering study of aluminium foams [19], as did Yamada et al. [20, 21] for microcellular magnesium alloys, that heat treatment can affect the foam very differently than it does the bulk alloy; 6xxx series aluminium alloys have been shown to display atypical intergranular failure when in microcellular form [22, 23] and local strut or cell wall properties have been found to differ from those of the same alloy in dense form [23, 24]; a fine-scale replicated microcellular Al–4.5 wt%Cu was shown to solidify and respond to ageing differently to the bulk alloy when the pore size falls below roughly 100 μm [15, 25]; since brittle second phases are frequently located near strut surfaces in microcellular alloys [17, 20, 26, 27]; internal damage accumulates differently during deformation in a microcellular structure than it does in the same alloy in bulk form.

Here, we examine whether the flow stress of replicated Al–4.5 wt%Cu displays the same relation between microstructure and flow stress, as it does in the dense alloy. Al–4.5 wt%Cu is a classical model alloy in metallurgical studies: it falls within a simple eutectic phase diagram, has been extensively studied from the standpoints of solidification, age-hardening and mechanical behaviour, and counts among the stronger cast engineering aluminium alloys [28, 29]. We vary its microstructure by producing the material at two different solidification rates and test the material in compression both before and after age-hardening, to explore how microstructural features affect the scaling relation between relative density (or porosity) and the flow stress of the material.

Experiments

Open-cell foams of aluminium alloyed with 4.5 wt% copper (containing 0.041 wt% Fe and 0.022 wt%Si, produced by Alusuisse in Neuhausen) were prepared by replication processing, as described in Refs. [1, 25, 30–32]. In brief, sieved monodisperse sodium chloride powder (99.5 % purity NaCl from Fluka Chemie GmbH, Buchs, Switzerland) with particles 400 μm in average diameter was packed, and cold isostatically pressed under pressures in the range of 30–45 MPa. These preforms were then infiltrated with molten Al–4.5 wt%Cu under argon gas at 0.4 MPa and then solidified under one of two conditions. The first, higher, cooling rate condition (hereafter designated as Condition A) corresponds to directional solidification of the NaCl/Al–4.5 wt%Cu composite over a copper chill, resulting in a cooling rate ranging from −30 to −22°/min (depending on distance from the chill). The second, lower, cooling rate (Condition C), corresponds to a much slower, homogeneous, cooling of the NaCl/Al–4.5 wt%Cu composite within the furnace, at −0.5 °C/min. The letters (A and C) correspond to those used in Ref. [25] to designate the same cooling conditions.

The solid Al–4.5 wt%Cu/NaCl composites were machined into cylinders 10 mm in diameter and 10-mm high for subsequent compression testing. The salt was then leached in a chromate conversion solution made of 1.62 g/l Na_2CrO_4 and 0.84 g/l $NaHCO_3$ in distilled water; this is a well-known corrosion inhibitor of aluminium in brine, used here to prevent aluminium hydroxide formation [33]. The resulting open-pore microcellular alloy samples have a relative density, V_m, situated at a prechosen and constant value between 0.12 and 0.25. Some samples were tested in the as-cast condition, while other samples were brought to the T6 condition by solution heat treatment at 525 °C for 4 h under argon, followed by quenching in water and age-hardening for 168 h at 130 °C under air. This heat treatment corresponds to peak of hardening of the alloy for this ageing temperature [15]. The four different microstructures tested are summarized in Table 1.

Compression testing was conducted using an MTS Alliance RT50 screw-driven testing machine, at a displacement rate of 5 μm/s (corresponding to a strain rate of 5×10^{-4} s^{-1}). The load was measured with a 5 kN load cell. The strain was measured using three LVDTs fixed 120° apart around the bottom compression plate and recording the displacement of the upper plate. Young's Modulus $E_f(e)$ was determined using the slope of load-

Table 1 The four Al–45 wt%Cu alloy processing conditions explored and their designation

Cooling condition		Condition A		Condition C
Cooling rate (°C/s)		−30 to −22		−0.5
Solidification time t_f (s)		200–270		12000
Age hardening	None	168 h at 130 °C (peak hardening)	None	168 h at 130 °C (peak hardening)
Designation	A	A + T6	C	C + T6

unload cycles performed at different values of the engineering strain e. The initial Young's modulus $E_{f,0}$ was determined by extrapolating the $E_f(e)$ curve to $e = 0$, as described in Ref. [6].

The mesostructure and the microstructure of the foam were examined by scanning electron microscopy (SEM) using a Philips XL 30 SEM operating at 15 kV and FEI Quanta Inspect 200LV equipped with EDAX, UTV detector and Genesis software. The metal microstructure was revealed by conventional metallographic preparation of porous or epoxy-infiltrated sections through samples of the microcellular alloy.

Results

Figure 1 shows SEM micrographs in electron backscattered mode of the four different microcellular Al–4.5 wt%Cu microstructures. The white phase corresponds to the θ (Al_2Cu) intermetallic and the light grey phase to primary α aluminium-copper solid solution. The as-cast microstructures obtained directly after infiltration (Conditions A and C) are shown on the left-hand side of Fig. 1. As documented for similar samples in Ref. [25], when solidified more rapidly (Condition A), the as-cast microstructure is dendritic in wider portions of metal. In narrower metal struts of the foam, the eutectic tends to be located either along the free surface (the former NaCl/alloy interface), or in narrow bands that cross the strut, Fig. 2. In samples solidified more slowly (Condition C), the dendritic character of the solidified metal microstructure is lost; the level of microsegregation is strongly reduced, and essentially all intermetallics are located along the surface of the struts, as is shown in Ref. [25].

In both conditions, one finds that the $\alpha + \theta$ eutectic is visible along the pore surface, Fig. 1. A systematic examination of roughly twenty samples in the electron microscope revealed no noticeable difference between the microstructures across the range of values of relative density, V_m, explored here: the average copper concentration within the struts, the gradient in copper concentration along the struts, as well as the fraction of struts crossed by eutectic (roughly one-half), show no visible dependence on V_m.

The microstructures of the heat-treated samples (A + T6 and C + T6) are seen on the right-hand side of Fig. 1: the amount of θ-phase is strongly reduced, while that portion which remains is coarser and primarily located along the pore surface. Thus, despite the solutionization treatment, intermetallics remain present.

After compression, the Al–4.5 wt%Cu foam shows traces of internal damage accumulation. This takes the form of cracking of intermetallic phases located along the foam surface and of strut buckling. Examples are given in Fig. 3 which shows SEM micrographs of an as-cast sample after compression.

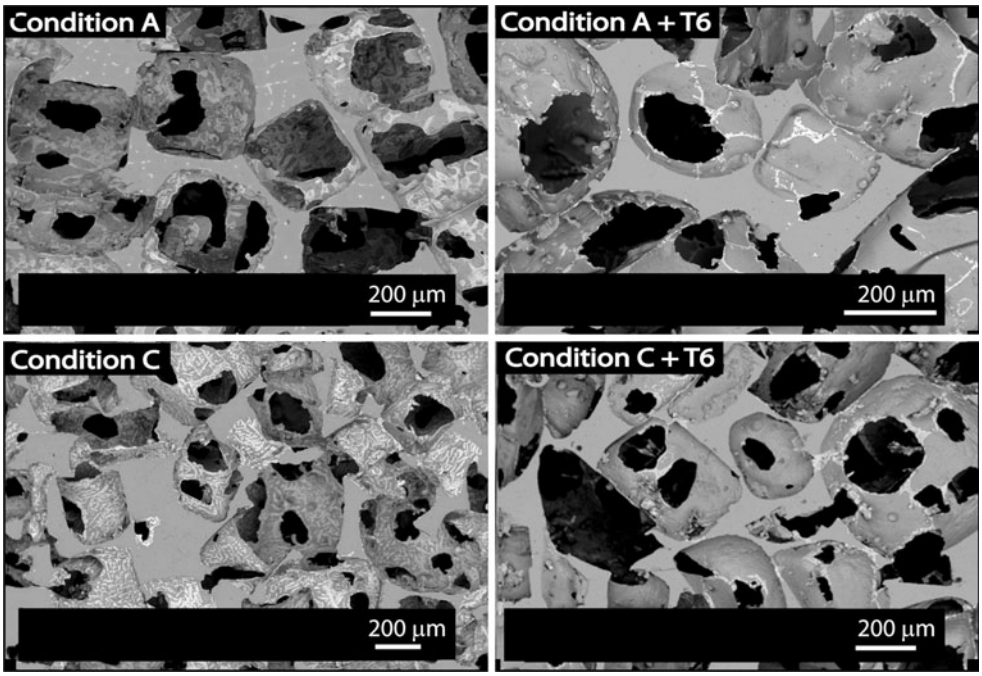

Fig. 1 Microstructure of the four different Al–4.5 %Cu foams. *Top left* (1): the as-cast material solidified more rapidly (*Condition A*). *Bottom left* (2): the as-cast material solidified slowly (*Condition C*). *Top right* (A + T6): heat-treated material solidified under *Condition A*. *Bottom right* (C + T6): heat-treated material solidified under *Condition C*

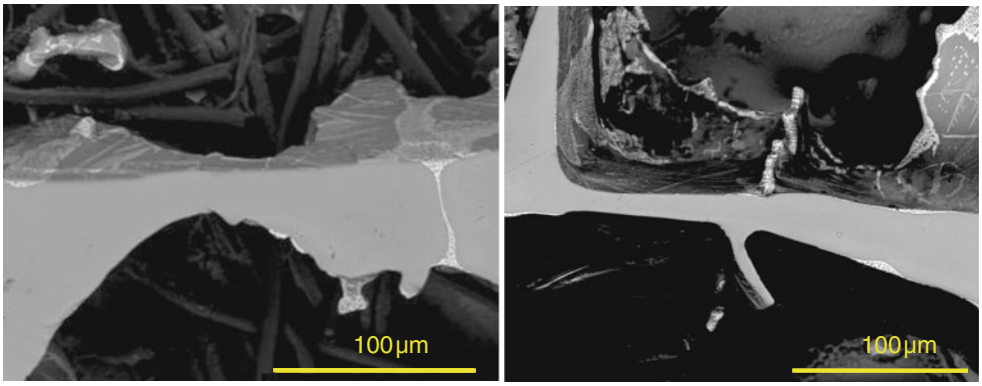

Fig. 2 Scanning electron micrographic close-ups of polished sections through individual struts in a non-deformed as-cast material of relative density 11 % solidified more rapidly (*Condition A*); micrographs show the θ-phase located along the strut surface and in one strut (*left*) crossing the strut

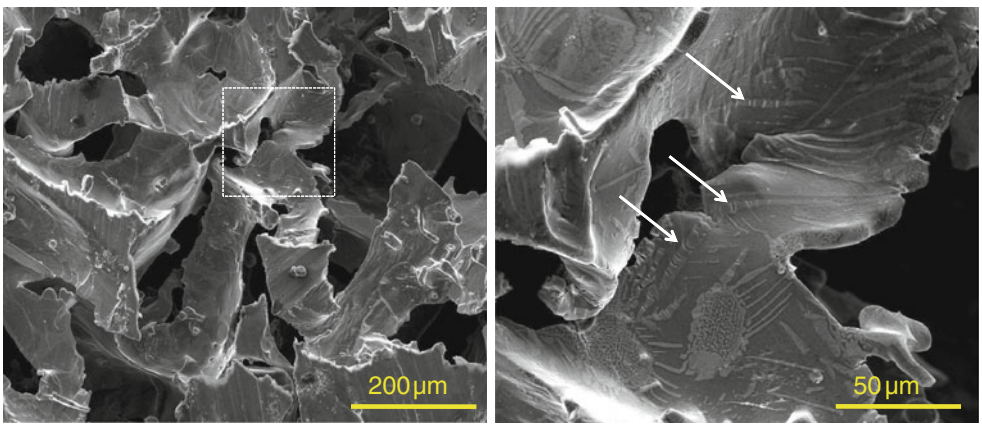

Fig. 3 Secondary electron SEM micrograph of the compressed as-cast Al–4.5 wt%Cu ($V_m = 11$ % deformed to 4 % strain) showing (*left*) deformed struts along the sample surface and the marked area at higher magnification (*right*) showing evidence of internal damage by microcracking of the intermetallic θ-phase (indicated with *white arrows*) as well as strut buckling

The foam Young's modulus $E_f(e)$ decreases as a function of the foam engineering strain e [6, 26, 30]. Figure 4 plots the initial Young's modulus, $E_{f,0}$, computed by extrapolation of $E_f(e)$ curves to $e = 0$ for each sample tested, versus foam relative density V_m. There is, as expected, no dependence on microstructure of the scaling law linking the modulus of the microcellular alloy with its relative density.

The rate of normalized stiffness decreases during compression, α, defined as

$$\alpha = \frac{1}{E_{f,0}} \frac{dE_f}{de} \quad (1)$$

averaged along each compression curve is an indicator of the rate at which internal damage accumulates within the foam as it deforms [26]. Figure 5 plots α for all four Al–4.5 %Cu foam microstructures versus V_m. Similar data for 99.99 % pure Al foams, from Ref. [34], are also plotted to show what obtains with a microstructure completely free of intermetallics. As seen, within the (significant) experimental scatter, no meaningful difference emerges neither between the four different alloyed foam structures, nor between these and microcellular pure aluminium.

Stress–strain curves of the microcellular alloy have the shape typical of replicated metal [1, 2] (see, for example, Fig. 4 of Ref. [6]). As is customary with microcellular materials [2, 3], the flow stress is a strong function of the relative density; this is seen in Fig. 6 which plots the flow stress of present samples at 3 or 5 % compressive strain versus V_m. Also given in the figure are corresponding data for similarly processed and tested samples of 99.99 % pure microcellular aluminium. The strong influence exerted by the relative density V_m on the flow stress is immediately apparent. Alloying and heat treatment also make a considerable difference, bringing the flow stress of the material in the same range as that of commercial aluminium-based foams, which have a better load-bearing (closed-cell) mesostructure than do replicated microcellular metals [2, 3]. Heat-treatment increases the flow stress by a factor near two, as was already reported in Ref. [15]; here again, there is no visible systematic difference between the two solidification conditions.

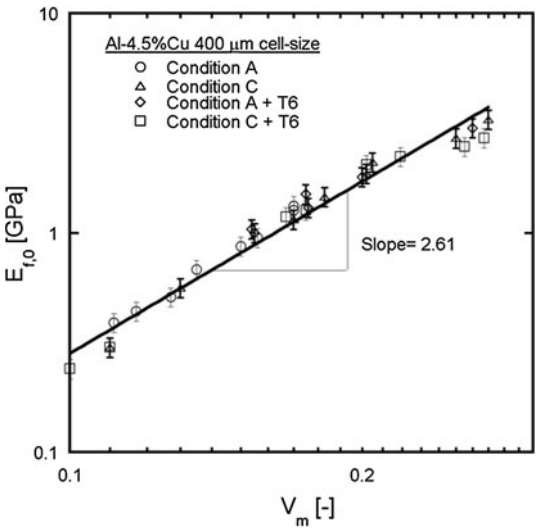

Fig. 4 Evolution of Young's modulus $E_{f,0}$ as a function of the relative density V_m for Al–4.5 %Cu foams with both the as-cast and T6 microstructures, for both cooling rates (*Conditions A* and *C*, Table 1). The log–log plot suggests a power-law relation of exponent near 2.6

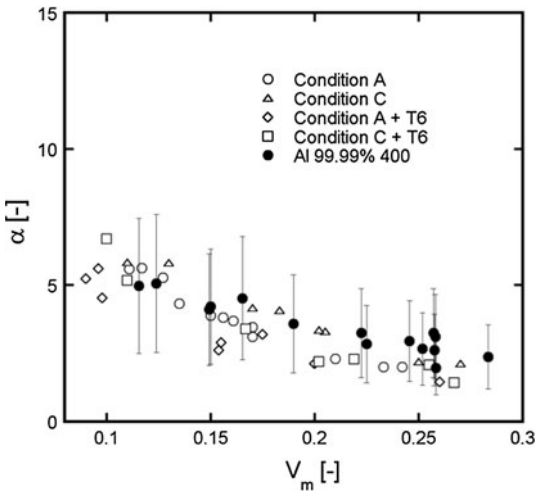

Fig. 5 Evolution of the damage parameter a with the relative density V_m, for Al–4.5 %Cu foams with the as-cast and T6 microstructures; the evolution of a for pure Al foams (measured in earlier work) is also shown. The experimental error on a is approximately of 50 %; for clarity, it is only shown on pure Al foams

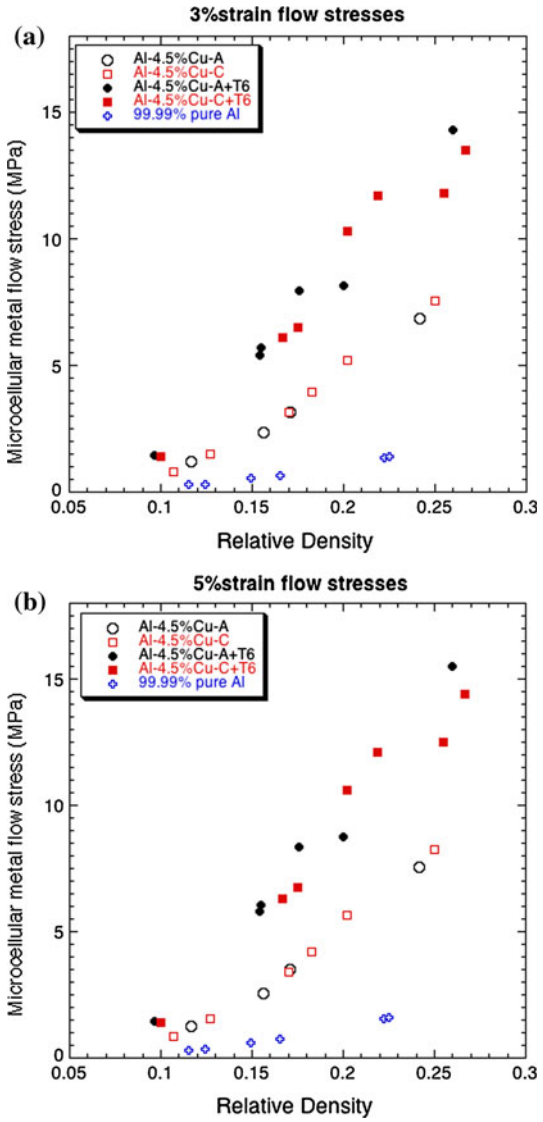

Fig. 6 Flow stress of all tested microcellular samples at 3 % (**a**) or 5 % (**b**) strain (in uniaxial compression) versus V_m. Also given in the figure are corresponding data for similarly processed and tested samples of 99.99 % pure microcellular aluminium

Discussion

Microstructure

As the alloy solidifies in the confined space between the NaCl particles, if cooling is slow the particles alter its microstructural development [25, 35]; this is observed here. Under Condition A, the microstructure is dendritic, with coring and interdendritic eutectic: it resembles that which would be found, at similar cooling rates, in the bulk alloy. At the lower solidification speed, Condition C, the dendritic character is lost. This is due to accelerated dendrite arm coalescence caused by the (NaCl) reinforcement. Simultaneously, microsegregation is strongly reduced by diffusion in the constrained solid α-phase. Present observations are consistent with earlier results on this system; we refer to Refs. [25, 35] for a detailed discussion and explanation of this microstructure.

When the Al–4.5 %Cu foams are heat-treated to the T6 state, most of the θ phase is dissolved; however, a certain fraction of intermetallic remains along the foam pore surfaces. That some residual intermetallic phases remain in the T6 microstructures, despite the high-temperature solutionisation heat treatment is explained by the presence of

iron impurities in the alloy. These form the essentially insoluble Al_7Cu_2Fe phase which remains after solutionization in the microcellular alloy, as was documented in earlier work [15].

Mechanical properties

The evolution of $E_{f,0}$ (Fig. 4) as a function of V_m follows a power-law scaling relation $E_{f,0} \propto V_m^N$ with $N \approx 2.6$. This is consistent with earlier studies of replicated aluminium foam over this range of relative density values [6, 30, 36]. Such consistency is expected: the elastic stiffness of metals and alloys is a relatively microstructure-independent property.

The flow stress of Al–4.5 %Cu foams is essentially doubled after age-hardening, as was already reported in Ref. [15]. The solidification rate has, on the other hand, essentially no influence on the flow stress of these open-cell foams. For the age-hardened foams, this is reasonable, as the heat-treatment homogenises the microstructure, erasing to a large extent the effect of solidification conditions. The result is, on the other hand, more surprising for the as-cast microstructures, given that the two solidification speeds produce markedly different microstructures (Fig. 1). Differences in coring level, different amounts of θ-phase and a difference in their scale or distribution thus apparently exert, in this system at least, little influence on the flow stress of the microcellular alloy.

Damage

All four Al–4.5 wt%Cu foams present a rate of stiffness loss, α, that is similar, within experimental error, to that of pure Al replicated foams, Fig. 5. This evolution of α is unlike that in replicated Al–12Si foam, which shows $\alpha \approx 10$ as a result of silicon particle cracking [26], or in Al–6.4 wt%Ni foam, for which α is again measurably above data for pure Al [37].

That α does not exceed in Al–4.5 wt%Cu foams, the value measured with pure Al is a priori surprising, since this alloy too contains brittle intermetallics (θ-Al_2Cu and Al_7Cu_2Fe) which fracture during foam deformation. The explanation is likely linked with the fact that θ-Al_2Cu and Al_7Cu_2Fe are mostly present as discrete islands along the pore surface (Figs. 1, 3). The fraction of applied load carried by the intermetallic is, therefore, far lower than in Al–12 %Si or Al–Ni alloy foams, where brittle second phases are more continuous and represent a higher volume fraction of the microstructure. Intermetallic fracture having apparently no noticeable influence on α; the rate of stiffness loss in Al–4.5 wt%Cu foams is thus by the same mechanisms as in pure Al replicated foams, namely bending and buckling of struts, Fig. 3 [6, 30].

Scaling of the flow stress

The variational estimate of Ponte-Castañeda and Suquet [38–43], adapted and simplified for the monotonic uniaxial deformation of (incompressible) non-linear microcellular materials [6, 44, 45], allows an estimation of the in situ stress–strain curves of the metal within the foams, knowing the relative density V_m, the Young's modulus scaling law and the uniaxial flow curve of the microcellular metal. The calculation is detailed in Appendix 1.

Figure 7a shows tensile curves measured on five samples of pure aluminium foam, produced by the same replication process as alloyed samples of this work and tested similarly. Figure 7b shows the back-calculated in situ stress–strain curves of the (pure Al) metal within these samples: as seen, the variational estimate collapses stress–strain curves of the five variously dense microcellular metal samples (Fig. 7a) into a single curve (Fig. 7b). This collapsed curve is, according to the model, the effective (von Mises) back-calculated in situ stress–strain curve of the metal making the foam—with the caveat that it is likely scaled down by a fixed 'knock-down' factor on the order of two to three, which has often been found in confronting data with theory but remains so far essentially unexplained [2, 6, 46, 47].

Save for this factor, the variational estimate thus provides a credible predictor of the scaling between the flow stress and the relative density of a replicated microcellular metal having a simple, essentially featureless, microstructure. It also performs well when confronted with steady-state creep data of replicated microcellular metal, as shown elsewhere [37, 48, 49].

Predictions of the model for the flow stress of the alloy are shown in Fig. 8. This plots the similarly back-calculated in situ flow stress of replicated microcellular Al–4.5 wt%Cu at 3 % (Fig. 8a) or 5 % (Fig. 8b) strain, together with the corresponding values for the pure Al samples.

The back-calculated flow stress for pure Al is single-valued across all values of V_m, consistent with Fig. 7, and the fact that the variational model accounts well for the observed scaling behaviour of the flow stress. It varies somewhat more but still remains relatively constant for heat-treated (T6) microcellular Al–4.5 wt%Cu when $V_m \geq 20$ %: the back-calculated in situ flow stress is within the ranges of 130–160 MPa at $\varepsilon_{eff} = 3$ %, 140–170 MPa at $\varepsilon_{eff} = 5$ %, Fig. 8. Note that these values are lower than the flow stress measured on dense castings of heat-treated Aluminium Alloy 201, of similar nominal composition 4.6 wt%Cu–0.7 wt%Ag–0.35 wt%Mn–0.35 wt%Mg–0.25 wt%Ti [29], which is in the range of 250–450 MPa after peak hardening [50]. This difference in flow stress, by a factor near two, is likely another example of the frequently reported 'knock-down' factor between

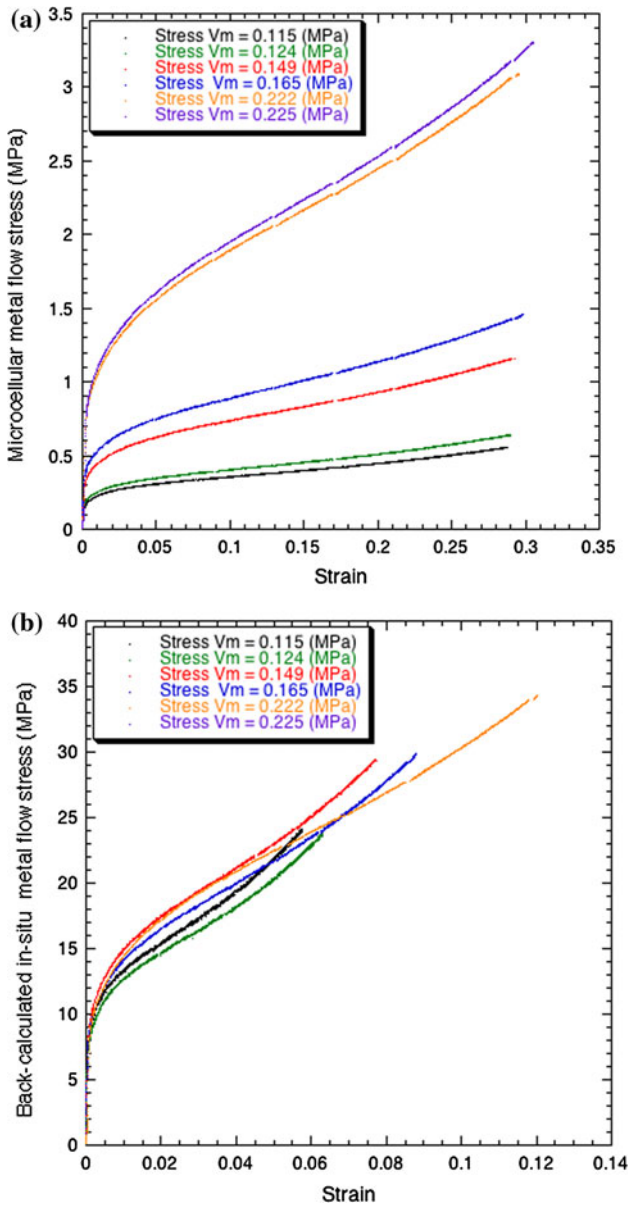

Fig. 7 **a** Measured flow curves of replicated 400-μm pore size microcellular 4 N pure aluminium; **b** back-calculated in situ strain–stress curves for pure Al in these replicated foams (using the variational estimate)

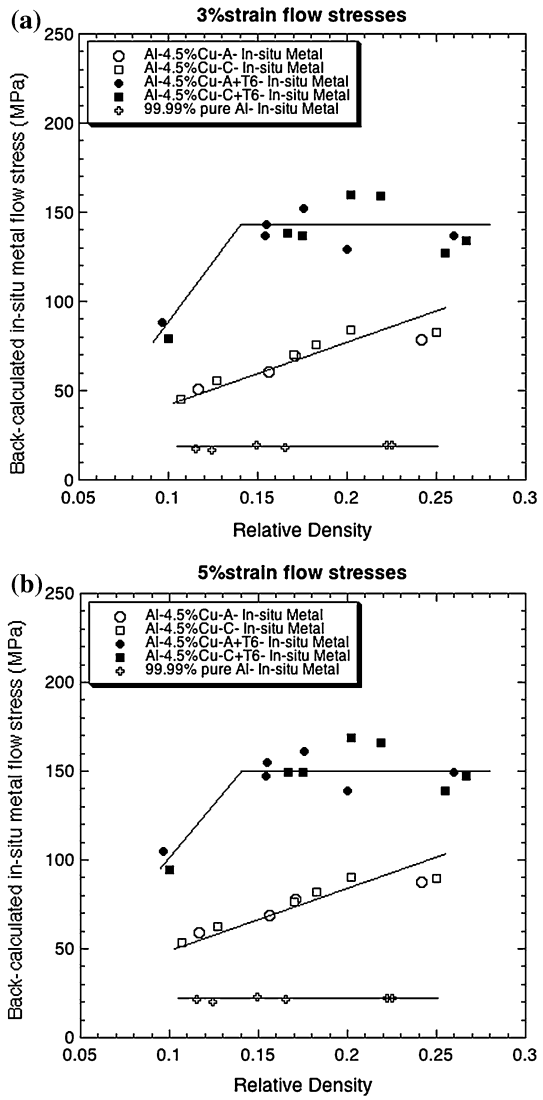

Fig. 8 Back-calculated in situ alloy flow stress in all tested microcellular samples at 3 % (**a**) or 5 % (**b**) effective strain versus V_m. Also given in the figure are corresponding data for similarly processed, tested and analysed samples of 99.99 % pure microcellular aluminium (also given in Figs. 6, 7)

theory and data for the plastic flow stress of microcellular materials [2, 6, 46, 47].

In other samples, the back-calculated flow stress decreases with the decreasing relative density. It falls below 100 MPa for the two heat-treated samples when $V_m \approx 0.1$, and it decreases steadily with the decreasing V_m for the as-cast samples in both the A and C conditions. Thus, the scaling relation that is predicted by the variational estimate is not obeyed by the alloyed metal in microcellular samples produced and tested here. This implies that their microstructure causes an additional dependence of the flow stress on relative density.

One potential cause for this was already mentioned in Ref. [6], namely internal damage. In applying the variational estimate, F (Eq. 6) was estimated on the basis of the initial Young's modulus of the foam, $E_{f,0}$, for two reasons: (i) the variational estimate is restricted to small-strain deformation and (ii) it is valid only for isotropic materials (the foam becomes anisotropic after significant deformation). In reality, E_f decreases with e at a rate that is measured by the damage parameter α (Eq. 1, Fig. 5). Looking at Eqs. 7 and 8, one sees that an overestimation of E_f, and hence of F, by a factor X ($X > 1$), will cause an underestimation of the back-calculated in situ metal flow stress σ_{eff} by a factor on the order of $X^{-1/2}$ (while the corresponding in situ strain ε_{eff} is overestimated by a factor on the order of

$X^{1/2}$, Appendix 1). Since $X \approx (1 - \alpha e)^{-1}$, this causes the in situ metal flow stress to be underestimated by a factor on the order of $(1 - \alpha e)^{1/2}$. At small strain and with α values in Fig. 5, the resulting error is on the order of a few percent; however, for, say, $e = 10$ % and $\alpha = 5$, then $X = 2$ and the flow stress are underestimated by a factor on the order of $\sqrt{2}$ (the theory being, besides, outside of its range of validity [2, 6, 45, 51]). At high α, therefore, internal damage offers one explanation for lower-than-expected back-calculated in situ alloy flow curves. Since α increases as V_m falls near 0.1 (Fig. 5; see also Fig. 8 of Ref. [37]), accelerated damage might contribute an explanation to the lower in situ flow stresses back-calculated for heat-treated microcellular Al–4.5 wt%Cu when $V_m \approx 0.1$.

This, however, does not explain why the in situ flow stress of the metal within the as-cast Al–4.5 %Cu foams varies monotonically with V_m, Fig. 7: α values are too low for this. Also, α is similar for pure Al or the alloy in all conditions; were it the cause for the observed decrease in apparent in situ flow stress for decreasing V_m, then pure Al and T6 alloy data should be similarly affected. This is not observed (Fig. 8). So there must be another cause for the decreasing in situ as-cast alloy flow stress with decreasing V_m.

The key difference between the metal in the as-cast microcellular Al–4.5 wt%Cu on one hand and Al–4.5 wt%Cu in the T6 condition or pure Al on the other is the heterogeneity of the as-cast alloy microstructure, for both cooling conditions: coring and second phases are present in the as-solidified alloy microstructure and are removed after heat-treatment, or are absent in the pure metal. As mentioned above, no systematic variation with V_m could be found in the microstructure of the solidified metal within the foams: the nature, size and distribution of phases are visibly the same, as are concentration gradients (these were estimated in several samples of different V_m using energy-dispersive X-ray analysis in the scanning electron microscope). In short, despite extensive investigation, no evolution of the microstructure could be found that would explain why the in situ metal flow stress decreases as V_m decrease.

We propose that the answer lies in the fact that, as V_m decreases with the alloy microstructure unchanged, the struts become thinner. This may cause the strut flow stress to evolve, since the nature and length-scale of the alloy microstructure remain constant and are commensurate in size with the strut width (a few μm). Indeed, if there are certain regions of the matrix microstructure that are weaker than the rest, then as V_m decreases, each weak region will locally represent a greater fraction of the strut cross-section, and hence cause a greater local weakening of the material wherever it appears.

Such weak regions are unlikely to be the brittle second phase θ, given that Young's modulus of the foams would also be affected (Fig. 5). Rather, these must be regions with a lower flow stress, but a modulus that remains near that of the metal. A likely culprit is the band of solute-poor metal that lines larger intermetallic phases; Fig. 9 shows such bands (a) within the microcellular alloy in a node and (b) within a portion of the strut shown in Fig. 2b. These are well-known (colour metallography reveals them well in Fig. 3 of Ref. [52]) and appear because, while Al–4.5 wt%Cu cools below the eutectic temperature, the solubility limit of copper within the primary α-phase decreases. Kinetics permitting, the amount of Al_2Cu intermetallic, therefore, increases as the alloy cools. This occurs either by diffusion and deposition of copper atoms onto existing (eutectic) θ-phase, or alternatively by nucleation and growth of new Al_2Cu, often visible as θ' platelets within the primary α-phase of the cast alloy. In the proximity of eutectic Al_2Cu, the former mechanism prevails, while

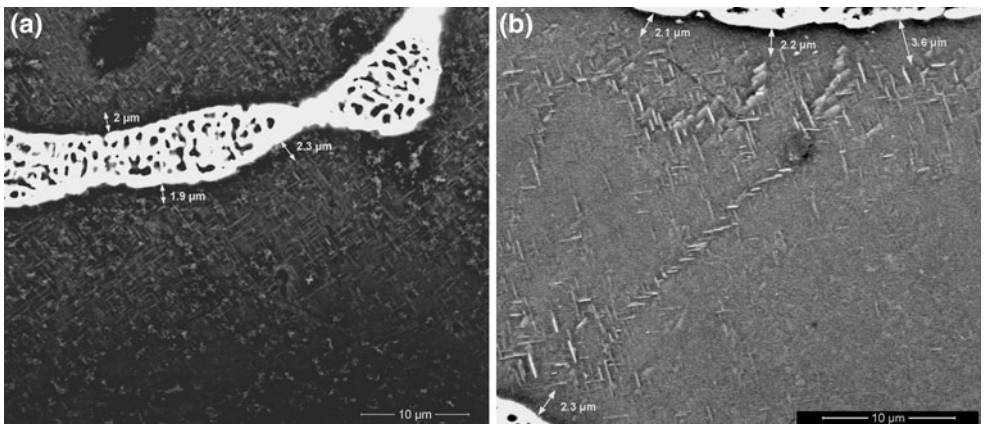

Fig. 9 **a** back-scattered SEM image of the as-cast Al-4.5 wt%Cu within a node of foam having $V_m = 0.17$, cooled under Condition A revealing the eutectic θ-phase and precipitated θ' platelets (*white*) within the primary aluminium-rich α-phase (*dark*). **b** portion of the strut in Fig. 2b, showing θ' platelets within the α-phase. In both θ' platelets are essentially absent within a band roughly 3-μm wide lining the (*white*) eutectic θ-phase; the band is indicated with *arrows* in both micrographs

further away from eutectic Al_2Cu, the latter mechanism dominates. The result is a band of softer precipitate-free copper-poor alpha-phase lining the eutectic θ-phase, the remainder of the alpha-phase containing a distribution of θ' platelets; such bands are shown in Fig. 9.

What this implies is that much of the surface of metal struts is lined with a band of copper-depleted (and hence softer) α-phase. Now the thickness of this band, on the order of a few micrometres (Fig. 9), is governed by the alloy cooling rate; it is independent of the strut thickness. As V_m decreases and with it the average thickness of struts within the microcellular material, such copper-depleted bands, therefore, represent an increasing proportion of the local struts cross-section, which can explain in turn why the apparent average in situ flow stress decreases as V_m decreases. The bands exist after both the A and C cooling conditions; it is hence reasonable that their effect be similar. After homogenization, alpha-phase concentration gradients are mostly erased, and these solute-poor bands are removed: this explains why there is much less of a spread with V_m in apparent metal in situ flow curves after heat-treatment, Fig. 8.

The more general implication is that the flow stress of microcellular metals (or materials more generally) can show unexpected scaling of their flow stress with relative density when the dimensional scale of pores (the mesostructure) and that of microstructural features within the base material (the microstructure) are commensurate. If the two do not scale similarly as the relative density changes, or if one is not much finer than the other, then the average in situ flow stress of the metal within the foam can vary with V_m, affecting in turn the scaling between relative density and strength for the microcellular metal.

In closing, we note that the effect shown here (i) has a parallel in the interplay among microstructure, mesostructure and strength that emerges from simulations of fracture in 2D microcellular structures by Mangipudi and Onck [53] and (ii) that it can be viewed as a manifestation of percolation size effects in the mechanical flow of materials: this is illustrated in Appendix 2 with a simple two-dimensional model.

Conclusions

- Replicated 400-μm pore size Al–4.5 %Cu foam solidified at one of two cooling conditions is tested in compression in the as-cast and age-hardened (T6) condition. At given relative density V_m, the yield strength is unaffected (within uncertainty) by the solidification rate; it increases by a factor near two after age-hardening.
- Brittle intermetallic phases (Al_2Cu and Al_7Cu_2Fe) are present in the two as-cast microstructures but are mostly dissolved after heat-treatment. Intermetallic phases are predominantly located along the foam pore surface. These fracture during foam compression; however, this does not influence the rate of Young's modulus decrease with foam strain.
- The in situ flow stress of the metal within the foams, back-calculated using the variational estimate knowing their modulus and the relative density V_m, is consistent for heat-treated Al–4.5 %Cu when $V_m \geq 0.2$, as is found also for pure Al. With the as-cast Al–4.5 %Cu in both conditions, the apparent average in situ metal flow stress increases with the increasing V_m. We propose that this is caused by the presence of a band of copper-depleted α-phase along the interface with intermetallics in the as-cast foam alloy; the thickness of these bands remaining constant, while the strut thickness decreases with decreasing V_m.
- When microstructural features of microcellular materials are of a size scale commensurate with that of their mesostructure, the scaling between relative density and flow stress can be altered compared to what obtains for a uniform elastoplastic continuum.

Acknowledgements This work was funded by the Swiss National Science Foundation, Project No. 200020-100179/1.

Appendices

Appendix 1: estimating the metal in situ flow curve from that of the foam knowing its Young's modulus, according to the simplified variational estimate

Assume that dislocation motion in the metal is governed by the second order moment of the instantaneous stress field in the metal making the foam, σ_{eff}. The rationale behind this assumption is that (i) the Von Mises stress is the simplest scalar measure of stress driving dislocation motion in complex three-dimensional stress fields and (ii) σ_{eff} is used, in the variational estimate, to deduce the appropriate matrix secant modulus that serves to derive the instantaneous non-linear deformation state in the metal making the foam [42, 43].

The variational estimate gives σ_{eff} from the volumetric average of the second order moment of the stress field in the linear comparison cellular material, which itself is related to the foam compliance M_e by [42, 43]

$$\sigma_{eff} = \left\{ \frac{3}{V_m} \left[s^* : \left(\frac{\partial M_e}{\partial (1/G_m)} \right)_{G_m = G_{ms}} : s^* \right] \right\}^{1/2}, \qquad (2)$$

where s^* is the instantaneous uniaxial stress applied monotonically to the porous foam material, and G_m is the (dense) metal shear modulus. Volume changes of

plastically deforming materials are very small, and high average hydrostatic stresses are unlikely in the matrix of a porous material: as in Ref. [6], we therefore assume that the metal matrix behaves as if it was incompressible. For uniaxial tensile deformation, Eq. 2 then simplifies to:

$$s^* = \sqrt{\frac{1-V_p}{3a}} \cdot \sigma_{eff} = \sqrt{\frac{V_m}{3a}} \cdot \sigma_{eff} \tag{3}$$

with

$$a = \left(\frac{\partial(1/E_f)}{\partial(1/G_m)} \right)_{G_m = G_{ms}}, \tag{4}$$

where G_{ms} is the secant shear modulus of the material making the foam at the relevant point of deformation of the foam. This is related to the secant Young's modulus E_{ms} of the (incompressible, dense) material by

$$E_{ms} = \frac{\sigma_{eff}}{\varepsilon_{eff}} = 3G_{ms}, \tag{5}$$

where ε_{eff} is the average equivalent strain that corresponds, according to the monotonic constitutive law of the material making the foam (in Von Mises terms its tensile uniaxial stress–strain curve), to the instantaneous value of σ_{eff} [54]. Now, the foam Young's modulus E_f is, for the given (isotropic) porous material mesostructure, equal to a certain fraction, F, of the Young's modulus E_m of the solid material making the foam:

$$E_f = FE_m, \tag{6}$$

where F is an increasing function of the relative density V_m of the foam. This being the case, Eq. 3 implies

$$\sigma_{eff} = \frac{s^*}{\sqrt{F_{(V_m)} V_m}}. \tag{7}$$

By definition of the secant modulus E_{fs} of the deforming foam:

$$e^* = \frac{s^*}{E_{fs}} = \frac{s^*}{F_{(V_m)} E_{ms}} = \frac{\sqrt{F_{(V_m)} V_m}}{F_{(V_m)}} \frac{\sigma_{eff}}{E_{ms}} = \sqrt{\frac{V_m}{F_{(V_m)}}} \varepsilon_{eff}, \tag{8}$$

where ε_{eff} is the matrix equivalent strain corresponding to the current equivalent stress, σ_{eff}, in the matrix (Eq. 2).

Therefore, if one plots, knowing the stress–strain curve (s^*, e^*) of the microcellular material, σ_{eff} as given in Eq. 7 versus

$$\varepsilon_{eff} = e^* \sqrt{\frac{F_{(V_m)}}{V_m}}, \tag{9}$$

then one recovers the monotonic stress–strain curve of the material making the foam, as estimated (under its assumptions) by the modified secant modulus method that corresponds to the variational estimate of Ponte-Castañeda and Suquet coupled with assumptions made above. For the present foams, from experimental data we have $F = 1.62 \cdot V_m^{2.61}$ (Fig. 4). Note that the above theory, and hence the estimated stress–strain curves are strictly only valid for isotropic materials under small strain deformation. The back-calculated curves are, therefore, strictly only valid at low values of e or ε_{eff}.

Appendix 2: illustrating how percolation size effects intervene when mesostructural and microstructural length scales are commensurate

Consider a strut in a foam made of a heterogeneous metal that is composed of softer zones and harder zones. At fixed pore size, when the relative density varies, the greatest change in mesostructure is that the struts making the foam become thinner. Assume a two-dimensional strut separated into a chequerboard assembly of rectangular elements, N elements across the width and M elements along the length of the beam, as schematized in Fig. 10. Each rectangular element is either soft or hard, with P the probability for an element to be soft. The shear flow stress τ as a function of shear strain γ in any given element is taken to be either:

$$\tau_i = \tau_{y,1} + \alpha_1 \gamma \quad \text{with probability } P \tag{10}$$

or

$$\tau_i = \tau_{y,2} + \alpha_2 \gamma \quad \text{with probability } (1-P) \tag{11}$$

with $\tau_{y,1}$ the yield shear stress and α_1 the strain hardening coefficient of the soft elements, and $\tau_{y,2}$ and α_2 the yield shear stress and strain hardening coefficient of the hard elements. For argument's sake, we give soft elements; the values corresponding to binary Al–1 %Cu, namely $\tau_{y,1} = 35$ MPa and $\alpha_1 = 100$ MPa, while for the hard elements, we take values typical of binary Al–4 %Cu, namely $\tau_{y,1} = 100$ MPa and $\alpha_1 = 750$ MPa [28].

We simplify loading of the beam as simple shear with the volume elements arranged as equal rectangles on a regular grid. We make the (simplistic) assumption that deformation of the beam occurs by isostrain deformation

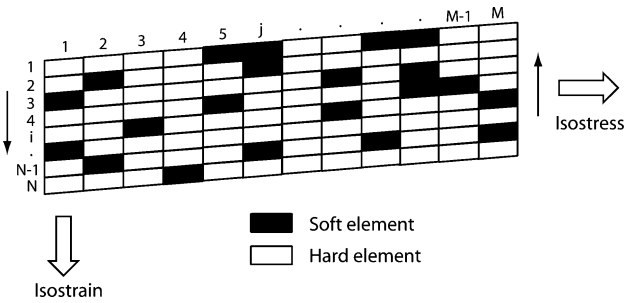

Fig. 10 Two dimensional beam made of random rectangular patches of soft and hard materials, the former being present with probability P, the latter with probability $(1 - P)$

across the beam and isostress deformation along the beam, as the assumed geometry suggests (Fig. 10). The average shear stress τ_j in line j at shear strain γ_j is then given by

$$\tau_j = \sum_{i=1}^{N} \frac{\tau_{y,i}}{N} + \frac{\alpha_i}{N}\gamma_j \tag{12}$$

if there are N elements across. This gives for γ_j, after rearrangement:

$$\gamma_j = \frac{N\tau_j - \sum_{i=1}^{N} \tau_{y,i}}{\sum_{i=1}^{N} \alpha_i}. \tag{13}$$

The average shear strain γ of the whole strut is then:

$$\gamma = \sum_{j=1}^{M} \frac{1}{M}\left[\frac{N\tau - \sum_{i=1}^{N} \tau_{y,i}}{\sum_{i=1}^{N} \alpha_i}\right], \tag{14}$$

if it is M elements long.

Calculations were conducted using a simple spreadsheet; the evolution of γ with the width of this fictive 2D strut is given in Fig. 11 for $\tau = 110$ MPa. The results correspond to an average over 20 struts with randomly generated elements for the relevant value of P. The bold line corresponds to the mean value of γ, and the thin lines show the standard deviation for the strain to which a single such 2D chequerboard beam will deform under $\tau = 110$ MPa. As seen, at high values of N, i.e., for thicker struts (high V_m), the values converge to a constant value, corresponding to an averaging over a large number of 'typical' random elements. For low values of N, i.e., for thinner struts (low V_m), γ tends to increase. This indicates a softening of the struts, or in other words a lowering of the average strut (and hence of the foam) flow stress. These trends are caused by the increased probability for soft zones to percolate across the width of thinner struts, which softens the entire beam at fixed phase proportions.

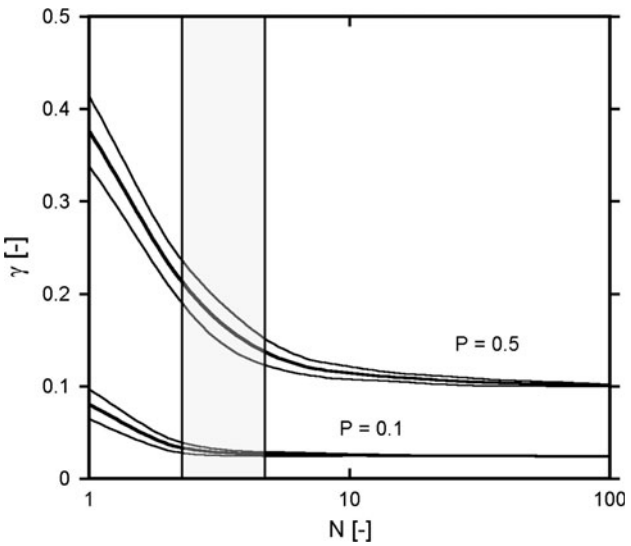

Fig. 11 Deformation of the rectangular beam in Fig. 10 at fixed applied stress versus its width (measured by the number of patches N) for two values of the soft phase probability P. Curves indicate the mean and standard deviation of 20 simulations for each condition

Figure 11 is drawn for two values of the probability P for the presence of a soft zone; one with a higher probability, $P = 0.5$ (to illustrate the as-cast structures, which contain a higher proportion of heterogeneity) and one with $P = 0.1$ to simulate the T6 microstructures (which have fewer sites of heterogeneity). As seen, for the same range of variation of the strut thickness (i.e., the same range of V_m values), one finds (i) a plateau, and then softening only at the lower end of the strut thickness range (and hence for the lowest V_m) in the material with fewer soft zones, and (ii) a regular decrease of the flow stress in the material with a greater proportion of softer regions. This simple model can thus reproduce quite faithfully all trends observed in the present experimental data (Fig. 8).

References

1. Conde Y, Despois JF, Goodall R et al (2006) Replication processing of highly porous materials. Adv Eng Mater 8:795–803
2. Goodall R, Mortensen A (2013) Porous metals. In: Hono K, Laughlin D (eds) Physical metallurgy, 5th edn. Elsevier, Amsterdam
3. Ashby MF, Evans A, Fleck NA, Gibson LJ, Hutchinson JW, Wadley HNG (2000) Metal foams: a design guide. Butterworth Heinemann, Boston
4. Tekoglu C, Gibson LJ, Pardoen T, Onck PR (2011) Size effects in foams: experiments and modeling. Prog Mater Sci 56:109–138. doi:10.1016/j.pmatsci.2010.06.001
5. Wadley HNG (2006) Multifunctional periodic cellular metals. Philos Trans R Soc A 364:31
6. Despois JF, Mueller R, Mortensen A (2006) Uniaxial deformation of microcellular metals. Acta Mater 54:4129–4142
7. Lehmhus D, Marschner C, Banhart J, Bomas H (2002) Influence of heat treatment on compression fatigue of aluminium foams. J Mater Sci 37:3447–3451. doi:10.1023/a:1016506905271
8. Lehmhus D, Banhart J (2003) Properties of heat-treated aluminium foams. Mater Sci Eng A 349:98
9. Feng Y, Tao N, Zhu Z, Hu S, Pan Y (2003) Effect of aging treatment on the quasi-static and dynamic compressive properties of aluminum alloy foams. Mater Lett 57:4058–4063
10. Zhou J, Gao Z, Cuitino AM, Soboyejo WO (2004) Effects of heat treatment on the compressive deformation behavior of open cell aluminum foams. Mater Sci Eng A 386:118–128
11. Zhou J, Soboyejo WO (2004) Compression-compression fatigue of open cell aluminum foams: macro-/micro-mechanisms and the effects of heat treatment. Mater Sci Eng A 369:23–35
12. Cao XQ, Wang ZH, Ma HQ, Zhao LM (2006) Effects of heat treatment on dynamic compressive properties and energy absorption characteristics of open-cell aluminum alloy foams. Trans Nonferrous Met Soc China 16:159–163. doi:10.1016/S1003-6326(06)60028-9
13. Amsterdam E, De Hosson JTM, Onck PR (2008) The influence of cell shape anisotropy on the tensile behavior of open cell

aluminium foam. Adv Eng Mater 10:877–881. doi:10.1016/j.scriptamat.2008.05.025
14. Amsterdam E, De Hosson JTM, Onck PR (2008) On the plastic collapse stress of open-cell aluminum foam. Scripta Mater 59:653–656. doi:10.1016/j.scriptamat.2008.05.025
15. Conde Y, Mortensen A (2008) Age-hardening response of replicated microcellular Al–4.5 %Cu. Adv Eng Mater 10:849–852. doi:10.1002/adem.200800086
16. Cluff DA, Esmaeili S (2008) Prediction of the effect of artificial aging heat treatment on the yield strength of an open-cell aluminum foam. J Mater Sci 43:1121–1127. doi:10.1007/s10853-007-2271-9
17. Campana F, Pilone D (2009) Effect of heat treatments on the mechanical behaviour of aluminium alloy foams. Scripta Mater 60:679–682. doi:10.1016/j.scriptamat.2008.12.045
18. Wang Z, Li Z, Ning J, Zhao L (2009) Effect of heat treatments on the crushing behaviour and energy absorbing performance of aluminium alloy foams. Mater Des 30:977–982. doi:10.1016/j.matdes.2008.06.058
19. Thornton PH, Magee CL (1975) The deformation of aluminum foams. Metall Trans 6A:1253–1263
20. Yamada Y, Shimojima K, Sakaguchi Y et al (2000) Effects of heat treatment on compressive properties of AZ91 Mg and SG91A Al foams with open cell structure. Mater Sci Eng A280:225–228
21. Kanahashi H, Mukai T, Yamada Y et al (2001) Experimental study for the improvement of the crashworthiness in az91 magnesium foam controlling its microstructure. Mater Sci Eng A308:283–287
22. Amsterdam E, Onck PR, De Hosson JTM (2005) Fracture and microstructure of open cell aluminum foam. J Mater Sci 40:5813
23. Zhou J, Allameh SM, Soboyejo WO (2005) Microscale testing of the strut in open-cell aluminum foams. J Mater Sci 40:429–439
24. Jeon I, Katou K, Sonoda T, Asahina T, Kang K-J (2009) Cell wall mechanical properties of closed-cell Al foam. Mech Mater 41:60–73. doi:10.1016/j.mechmat.2008.08.002
25. Conde Y, Mortensen A (2010) Solidification of Al–4.5 wt %Cu-replicated foams. Met Mater Trans A 41:2048–2055
26. San Marchi C, Despois JF, Mortensen A (2004) Uniaxial deformation of open-cell aluminum foam: the role of internal damage. Acta Mater 52:2895–2902
27. Fischer SF, Schüler P, Fleck C, Bührig-Polaczek A (2013) Influence of the casting and mould temperatures on the (micro)structure and compression behaviour of investment-cast open-pore aluminium foams. Acta Mater 61:5152–5161. doi:10.1016/j.actamat.2013.04.069
28. Mondolfo LF (1976) Aluminum alloys: structure and properties. Butterworths, London
29. Davis JR (ed) (1998) Metals handbook, desk edition, 2nd edn. ASM International, Metals Park
30. San Marchi C, Mortensen A (2001) Deformation of open-cell aluminum foam. Acta Mater 49:3959–3969
31. San Marchi C, Mortensen A (2002) Infiltration and the replication process for producing metal sponges. In: Degischer HP, Kriszt B (eds) Handbook of cellular metals. Wiley, Weinheim
32. Despois JF, Marmottant A, Conde Y et al (2006) Microstructural tailoring of open-pore microcellular aluminium by replication processing. Mater Sci Forum 512:281–288
33. Diologent F, Goodall R, Mortensen A (2009) Surface oxide in replicated microcellular aluminium and its influence on the plasticity size effect. Acta Mater 57:286–294
34. J-F Despois (2005) EPFL Thesis number 3268, Institute of Materials, Ecole Polytechnique Fédérale de Lausanne, Lausanne, Switzerland
35. Mortensen A, Flemings MC (1996) Solidification of binary hypoeutectic alloy matrix composite castings. Metall Mater Trans 27A:595–609
36. Goodall R, Marmottant A, Salvo L, Mortensen A (2007) Spherical pore replicated microcellular aluminium: processing and influence on properties. Mater Sci Eng A 465:124–135. doi:10.1016/j.msea.2007.02.002
37. Diologent F, Conde Y, Goodall R, Mortensen A (2009) Microstructure, strength and creep of aluminium–nickel open cell foam. Philos Mag 89:1121–1139
38. Ponte-Castañeda P (1991) The effective mechanical properties of nonlinear isotropic composites. J Mech Phys Solids 39:45–71
39. Michel JC, Suquet PM (1992) The constitutive law of nonlinear viscous and porous materials. J Mech Phys Solids 40:783–812
40. Suquet PM (1993) Overall potentials and extremal surfaces of power law or ideally plastic composites. J Mech Phys Solids 41:981–1002
41. Suquet PM (1995) Overall properties of nonlinear composites: a modified secant moduli theory and its link with Ponte Castaneda's nonlinear variational procedure. Comptes Rendus de l'Académie des Sciences de Paris 320:563–571
42. Suquet P (1997) Effective properties of nonlinear composites. In: Suquet P (ed) Continuum micromechanics. Springer, New York
43. Ponte-Castañeda P, Suquet P (1998) Nonlinear composites. Adv Appl Mech 34:171–302
44. Mueller R, Mortensen A (2006) Simplified prediction of the monotonic uniaxial stress–strain curve of non-linear particulate composites. Acta Mater 54:2145
45. Mueller R, Soubielle S, Goodall R, Diologent F, Mortensen A (2007) On the steady-state creep of microcellular metals. Scripta Mater 57:33
46. Gibson LJ, Ashby MF (1997) Cellular solids: structure and properties, 2nd edn. Cambridge University Press, Cambridge
47. Diologent F, Goodall R, Mortensen A (2011) Activation volume in microcellular aluminium: size effects in thermally activated plastic flow. Acta Mater 59:6869–6879. doi:10.1016/j.actamat.2011.07.021
48. Diologent F, Goodall R, Mortensen A (2009) Creep of aluminium–magnesium open cell foam. Acta Mater 57:830
49. Soubielle S, Diologent F, Salvo L, Mortensen A (2011) Creep of replicated microcellular aluminium. Acta Mater 59:440–450. doi:10.1016/j.actamat.2010.09.037
50. Moosbrugger C (ed) (2002) Atlas of stress–strain curves. ASM International, Materials Park
51. Mangipudi KR, van Buuren SW, Onck PR (2010) The microstructural origin of strain hardening in two-dimensional open-cell metal foams. Int J Solids Struct 47:2081–2096. doi:10.1016/j.ijsolstr.2010.04.009
52. Mortensen A, Gungor MN, Cornie JA, Flemings MC (1986) Alloy microstructures in cast metal matrix composites. J Met 38:30–35
53. Mangipudi KR, Onck PR (2011) Multiscale modelling of damage and failure in two-dimensional metallic foams. J Mech Phys Solids 59:1437–1461. doi:10.1016/j.jmps.2011.02.008
54. Berveiller M, Zaoui A (1978) An extension of the self-consistent scheme to plastically-flowing polycrystals. J Mech Phys Solids 26:325–344